Nuclear Ignition of White Dwarf Stars by Relativistic Encounters with Rotating Intermediate Mass Black Holes

5 authors, including:

P. Chris Fragile
College of Charleston
136 PUBLICATIONS   **4,408** CITATIONS

Nuclear Ignition of White Dwarf Stars by Relativistic Encounters with Rotating Intermediate Mass Black Holes

PETER ANNINOS,[1] ROBERT D. HOFFMAN,[1] MANVIR GREWAL,[2] MICHAEL J. LAVELL,[1] AND P. CHRIS FRAGILE[3, 4]

[1] *Lawrence Livermore National Laboratory, Livermore, CA 94550, USA*
[2] *Department of Physics, Columbia University, New York, NY 10027, USA*
[3] *Department of Physics and Astronomy, College of Charleston, Charleston, SC 29424, USA*
[4] *Kavli Institute of Theoretical Physics, University of California at Santa Barbara, Santa Barbara, CA 93106, USA*

ABSTRACT

We present results from general relativistic calculations of nuclear ignition in white dwarf stars triggered by near encounters with rotating intermediate mass black holes with different spin and alignment parameters. These encounters create thermonuclear environments characteristic of Type Ia supernovae capable of producing both calcium and iron group elements in arbitrary ratios, depending primarily on the proximity of the interaction which acts as a strong moderator of nucleosynthesis. We explore the effects of black hole spin and spin-orbital alignment on burn product synthesis to determine whether they might also be capable of moderating reactive flows. When normalized to equivalent impact penetration, accounting for frame dragging corrections, the influence of spin is weak, no more than 25% as measured by nuclear energy release and mass of burn products, even for near maximally rotating black holes. Stars on prograde trajectories approach closer to the black hole and produce significantly more unbound debris and iron group elements than is possible by encounters with nonrotating black holes or by retrograde orbits, at more than 50% mass conversion efficiency. The debris contains several radioisotopes, most notably ^{56}Ni, made in amounts that produce sub-luminous (but still observable) light curves compared to branch-normal SNe Ia.

Keywords: Black holes — White dwarf stars — Black hole physics — Hydrodynamics — Explosive nucleosynthesis

1. INTRODUCTION

The tidal disruption (TD) of white dwarf (WD) stars by intermediate mass black holes (IMBH) are violent cosmic events capable of generating observable electromagnetic and gravitational wave energies (Rees 1988; Haas et al. 2012; MacLeod et al. 2016). One particularly intriguing aspect of TD events is the possibility that compressive forces exerted by the BH might trigger explosive thermonuclear reactions inside the WD, producing isotopically rich environments composed of both intermediate and iron-group nuclei (Luminet & Pichon 1989; Rosswog et al. 2009). If sufficient amounts of radioactive nuclei are synthesized and dispersed among unbound debris, their decay and subsequent reprocessing could give rise to observable transient emissions. And if these signatures are clearly distinguishable from other known transient patterns (e.g., Type Ia supernovae) they will provide strong evidence to the existence of IMBHs and help determine their mass function (Gerssen et al. 2002, 2003; Gebhardt et al. 2002, 2005; Dong et al. 2007).

A host of simulated WD-IMBH binary systems have demonstrated that indeed explosive nucleosynthesis is a likely outcome for events with sufficiently large tidal strength, defined as $\beta = R_T/R_P$, the ratio of tidal to perihelion radii (Rosswog et al. 2009; Tanikawa et al. 2017; Kawana et al. 2018; Anninos et al. 2018). The precise ignition threshold depends on the WD mass, but a general requirement is $\beta > 3$ (5) for the more (less) massive WD stars. These scenarios additionally have the potential to release more nuclear energy than the star's quiescent binding energy and give rise to short-burst accretion rates of up to 10^7 - $10^8 M_\odot$ yr^{-1} (Haas et al. 2012; Anninos et al. 2018). For weaker or greater perihelion radius interactions, nucleosynthesis might still occur but not as efficiently. The outcome in these cases will likely produce calcium-rich (as opposed to iron-rich) debris depending on the WD mass and interaction strength (Holcomb et al. 2013; Sell et al. 2015; Anninos et al. 2018). These conclusions are gathered from a collective body of calculations that considered somewhat idealized WD-IMBH configurations and (for the most part) pseudo-Newtonian interactions. The effects of BH spin and spin-axis orientation on the thermonuclear environment of the

WD, for example, have not been investigated. Black hole spin was considered by Haas et al. (2012) and Evans et al. (2015) with general relativity, and by Gafton & Rosswog (2019) with a generalized Newtonian method, but none of those studies included reactive networks in their calculations.

Here we study nuclear processes triggered by the disruption of WD stars by close encounters with rotating and tilted IMBHs, i.e. BHs with spin axes not aligned perpendicular to the orbital plane. Our goal is to extend previous work by considering a broader range of interaction scenarios, and account for general relativistic effects expected from near encounters. To this end, we use a combined moving mesh and adaptive mesh refinement (AMR) capability that we developed specifically for this problem class (Anninos et al. 2012, 2018). The AMR/moving mesh hybrid approach allows us to move the base grid along Lagrangian fluid lines, simultaneously following the Keplerian trajectory and compression of the WD stars while at the same time refining on the densest parts of the stars as they compress and stretch from tidal forces. The enhanced grid resolution made possible by this hybrid adaptive approach is critical in order to achieve sufficient zone resolution along the orbital plane and provide the necessary scale height coverage to resolve reactive flows and internal shock features (Tanikawa et al. 2017). Our numerical methods and calculations are implemented and carried out in a background metric approximation. We solve the general relativistic hydrodynamics equations in a background Kerr-Schild spacetime written in Cartesian coordinates, modified to account for the evolving gravitational potential of the white dwarf, and coupled with an α-chain nuclear network and burn energy coupling.

We begin in Section 2 with a brief discussion of our numerical methods, physical models (equation of state, reactive networks, initial data, etc.), and dynamic mesh strategy tuned to approach the high spatial resolution required for resolving nucleosynthesis. Our results follow in Section 3, and we conclude with a brief summary in Section 4.

2. METHODS AND MODELS

All calculations are performed with the COSMOS++ code (Anninos et al. 2005; Fragile et al. 2012, 2014; Anninos et al. 2017), which solves the equations of general relativistic hydrodynamics coupled with thermonuclear reactions and energy generation on unstructured, moving and adaptively refined (AMR) meshes. Except for one addition to be described immediately below, the combined AMR and grid motion strategy is for the most part identical to what we presented in Anninos et al. (2012, 2018), so we do not repeat those details here. We do however remind the reader that our highest resolution calculations use a base grid of 96^3 cells and two additional refinement levels for an effective 384^3 resolution of $\sim 10^7$ cm along the x and y coordinates within the orbital plane. Our vertical mesh motion strategy additionally follows the Lagrangian compression down to a scale of $\lesssim 10^6$ cm (or equivalently 1/300th of a Schwarzschild radius) along the z axis perpendicular to the orbital plane.

The domain of the grid is initially constructed to cover 10 (5) stellar radii parallel (perpendicular) to the orbital plane, but we emphasize that the domain extent varies in both time and space as the mesh velocity adjusts anisotropically to follow tidal debris. Boundary conditions for the hydrodynamics on the outer edges of the grid are set to outflow: all ghost zone quantities are equated to the values of their adjacent internal-zone neighbors, except the velocity component normal to the boundary is set to zero if it points onto the grid. We use multipole boundary conditions for the gravitational potential, up to and including 10 moments. The time step is limited by the minimum stability criteria for the hydrodynamics, dynamical self-gravity, nuclear energy production, and fractional abundance changes (Anninos et al. 2018).

In order to accommodate the possibility that an arbitrarily aligned BH spin axis might entrain material off the orbital plane we have generalized the vertical grid motion to expand the mesh if the stellar boundary (defined as 10^{-3} of the peak density) is detected near the outer grid boundaries. This is accomplished by setting the vertical mesh velocity component to

$$|V_g^z(t)| = \chi_0 \ |V_L^z(t)| \ \left| \frac{z(t)}{L_z(t)} \right|^{\chi_N} , \tag{1}$$

where $z(t)$ is the time-dependent coordinate, $L_z(t)$ is the changing vertical length of the grid along the positive z-axis (distance from the orbital plane to the outer boundary), $\chi_0 \geq 0$ is a constant multiplier, and $|V_L^z(t)|$ is the magnitude of the z-component of the star's maximum outward-directed Lagrangian velocity. The factor $|z(t)/L_z(t)|^{\chi_N}$ smoothly scales back the vertical grid motion to zero at the midplane, preventing loss of resolution in and around the orbital plane. Values of the exponent χ_N greater (less) than unity tend to move the outer grid edges faster (slower) than the midplane cells. We find $\chi_N = 1.2$ and $\chi_0 = 0.25$ work reasonably well. This grid velocity component is applied symmetrically above and below the midplane, but only for tilted spin cases and only when significantly overdense material reaches the boundaries. Equation(1) is similar in form to what we use for collapsing the mesh onto the orbital

plane at early times, but we now also adapt it (with different parameter sets) to expand the mesh and track off-plane entrainment.

In addition to generalizing the mesh motion strategy to accommodate off-plane entrainment, we have made a number of other significant improvements to the physical models. The most important of which is a more accurate equation of state (EOS), upgraded from an idealized 2-state (hot, cold) and 2-component (ion, radiation) treatment to a Helmholtz model suited for representing electron degeneracy and relativistic and electron-positron contributions. Our implementation is based on the Torch code (Timmes 1999; Timmes et al. 2000a) and is designed to work with arbitrary isotopic compositions and can be coupled to nuclear reaction networks as we have done for this work. The Helmholtz EOS is utilized in tabular form with densities spanning the range $10^{-12} \leq \rho \leq 10^{15}$ gm cm^{-3}, and temperatures $10^3 \leq T \leq 10^{13}$ K. Interpolations between table entries are performed with biquintic Hermite polynomials that ensures thermodynamic consistency.

Another improvement concerns the development of a particle tracer capability that we use to sample and track stellar material and its thermodynamic state (density, temperature, energy) as it evolves in space and time. This data (consisting of tens of thousands of particles) is stored at regular cyclic intervals and, upon completion of the calculations, is input to a stand-alone network solver code for post-processing with a much larger and more accurate nuclear reaction network than is possible inline. For the inline network we use the same 19-isotope α-chain and heavy-ion reaction model that we used previously (Weaver et al. 1978; Timmes 1999; Timmes et al. 2000b; Anninos et al. 2018). It is fully coupled with the relativistic hydrodynamics equations, including isotopics and nuclear energy released. The 19-isotope network was the main diagnostic we relied on for calculating burn products in our previous work. We continue to rely on this model for nuclear energy feedback to the hydrodynamics, but now we use the off-line post-processing capability to calculate more detailed isotopic compositions using a version of the Torch code (Timmes 1999) that we modified for parallel processing.

We have also accounted for self-gravity beyond the quasi-static Cowling approximation used in our previous work. This is done by solving for the gravitational potential (ϕ) of the WD in an asymptotically flat spacetime at each time cycle, then adding it as a first order perturbation to the Cartesian Kerr-Schild metric, which we write in *untilted* form assuming unit light speed

$$ds^2_{(\mathrm{KS})} = (\eta_{\mu\nu} + f p_\mu p_\nu) dx^\mu dx^\nu = -(1-f) dt^2 + (f p_i) dt dx^i + (\delta_{ij} + f p_i p_j) dx^i dx^j \ , \tag{2}$$

where $f = 2 G M_{\mathrm{BH}} \tilde{r}^3 / (\tilde{r}^4 + a^2 \tilde{z}^2)$, M_{BH} is the BH mass, a is its spin, p_i are the spin modified directional cosines

$$
\begin{aligned}
p_0 &= 1 \ , \\
p_x &= (\tilde{r}\tilde{x} + a\tilde{y})/(\tilde{r}^2 + a^2) \ , \\
p_y &= (\tilde{r}\tilde{y} - a\tilde{x})/(\tilde{r}^2 + a^2) \ , \\
p_z &= \tilde{z}/\tilde{r} \ ,
\end{aligned}
\tag{3}
$$

$\tilde{x}^i$ define the tilted coordinates

$$
\begin{aligned}
\tilde{x} &= x \cos(\zeta) + z \sin(\zeta) \ , \\
\tilde{y} &= y \ , \\
\tilde{z} &= -x \sin(\zeta) + z \cos(\zeta) \ ,
\end{aligned}
\tag{4}
$$

and

$$
\begin{aligned}
\tilde{r}^2_* &= \tilde{x}^2 + \tilde{y}^2 + \tilde{z}^2 - a^2 \ , \\
\tilde{r}^2 &= \frac{1}{2}(\tilde{r}^2_* + \sqrt{\tilde{r}^4_* + 4 a^2 \tilde{z}^2} \ ) \ .
\end{aligned}
\tag{5}
$$

ζ is the angle of tilt that we have arbitrarily assigned around the y axis. The complete *tilted* spacetime metric is written in terms of the *untilted* metric as

$$
\begin{aligned}
g^{(\mathrm{TKS})}_{00} &= g^{(\mathrm{KS})}_{00} \ , \\
g^{(\mathrm{TKS})}_{02} &= g^{(\mathrm{KS})}_{02} \ ,
\end{aligned}
$$

$$
\begin{aligned}
g_{22}^{\text{(TKS)}} =& g_{22}^{\text{(KS)}} \ , \\
g_{01}^{\text{(TKS)}} =& \cos(\zeta) g_{01}^{\text{(KS)}} - \sin(\zeta) g_{03}^{\text{(KS)}} \ , \\
g_{12}^{\text{(TKS)}} =& \cos(\zeta) g_{12}^{\text{(KS)}} - \sin(\zeta) g_{23}^{\text{(KS)}} \ , \\
g_{03}^{\text{(TKS)}} =& \sin(\zeta) g_{01}^{\text{(KS)}} + \cos(\zeta) g_{03}^{\text{(KS)}} \ , \\
g_{23}^{\text{(TKS)}} =& \sin(\zeta) g_{12}^{\text{(KS)}} + \cos(\zeta) g_{23}^{\text{(KS)}} \ , \\
g_{11}^{\text{(TKS)}} =& \cos(\zeta)\cos(\zeta) g_{11}^{\text{(KS)}} + \sin(\zeta)\sin(\zeta) g_{33}^{\text{(KS)}} - (\sin(\zeta)\cos(\zeta) + \sin(\zeta)\cos(\zeta)) g_{13}^{\text{(KS)}} \ , \\
g_{13}^{\text{(TKS)}} =& \cos(\zeta)\sin(\zeta) g_{11}^{\text{(KS)}} - \cos(\zeta)\sin(\zeta) g_{33}^{\text{(KS)}} + (\cos(\zeta)\cos(\zeta) - \sin(\zeta)\sin(\zeta)) g_{13}^{\text{(KS)}} \ , \\
g_{33}^{\text{(TKS)}} =& \sin(\zeta)\sin(\zeta) g_{11}^{\text{(KS)}} + \cos(\zeta)\cos(\zeta) g_{33}^{\text{(KS)}} + (\sin(\zeta)\cos(\zeta) + \sin(\zeta)\cos(\zeta)) g_{13}^{\text{(KS)}} \ .
\end{aligned}
\tag{6}
$$

Neglecting high order corrections that come from spin and near-field effects, the WD potential contributes to the scalar curvature components of the metric in the manner $g_{\mu\nu} = \eta_{\mu\nu} + f p_\mu p_\nu - 2\phi \delta_{\mu\nu}$, so that the line element becomes finally

$$
ds^2 = \left(g_{00}^{\text{(TKS)}} - 2\phi \right) dt^2 + \left(g_{0i}^{\text{(TKS)}} \right) dt dx^i + \left(g_{ij}^{\text{(TKS)}} - 2\phi \delta_{ij} \right) dx^i dx^j \ .
\tag{7}
$$

We find this to be a reasonable approximation that maintains equilibrium outside of the tidal radius. Of course it is increasingly less accurate near the BH, but there it is also less important. We apply the perturbation potential early on in an encounter until the WD approaches to about a half tidal radius of the BH, at which point self-gravity can be safely ignored to speed up the calculations.

This treatment of the spacetime metric provides flexibility for the alignment of the BH spin axis while confining the WD trajectory to the $z = 0$ plane. Alignment of the WD trajectory to one of the principle axes of the grid mitigates some of the effects of numerical dissipation and mesh imprinting on its evolution that would be more strongly present if the WD were to travel along the cell diagonals, which would be the case if we had instead chosen to align the BH spin axis to the grid. It also simplifies the grid motion strategy for collapsing zones along Lagrangian fluid lines orthogonal to the orbital plane.

2.1. *Initial Data*

In Anninos et al. (2018), henceforth referred to as Paper 1, we considered 0.2 and 0.6 solar mass WD stars approaching nonrotating intermediate mass black holes, varying the perihelion distance to achieve tidal strengths between $2.6 \leq \beta \leq 17$. Here we extend the interaction parameter space by considering black holes with different spins and rotation axis orientations (tilt) to see if correlations exist between these parameters and nuclear activity. In order to reduce the number of calculations to a manageable level, we constrain the parameter space to two basic scenarios: a $0.6 M_\odot$ (CO) WD approaching a $10^3 M_\odot$ BH (case A), and a $0.15 M_\odot$ (He) WD approaching a $10^4 M_\odot$ BH (case B). Black hole spin is additionally limited to either zero or 0.9 (in BH mass units, where 1 is a maximally rotating Kerr BH), and three tilt configurations corresponding to retrograde, polar, and prograde orbital alignments.

Although our maximum spin case has an a/M that is less than the theoretical maximum of 0.998 (Thorne 1974), a value close to 0.9 is more consistent with estimates of realistic spin equilibrium values that account for spin-up and spin-down processes (Gammie et al. 2004). Furthermore, techniques for measuring black hole spin have yet to converge, with the Fe-line fitting method tending to favor high spins ($a/M \gtrsim 0.8$) (Reynolds 2014), the thermal spectral fitting method favoring more modest spins ($0.2 \lesssim a/M \lesssim 0.9$) (McClintock et al. 2014), and early gravitational wave detections possibly suggesting very low spins ($|a/M| \leq 0.3$) (Farr et al. 2017). Given this uncertainty, $a/M = 0.9$ seems like a safe, and reasonable, value to consider.

We also limit our studies to a narrow range of interaction strengths $4.4 \leq \beta \leq 6.8$, where β is the ratio of tidal to perihelion radii $\beta = R_T / R_P$, with tidal radius

$$
R_{\text{T}} \approx 1.2 \times 10^5 \left(\frac{R_{\text{WD}}}{10^9 \text{cm}} \right) \left(\frac{M_{\text{BH}}}{10^3 M_\odot} \right)^{1/3} \left(\frac{M_{\text{WD}}}{0.6 M_\odot} \right)^{-1/3} \text{km} \ ,
\tag{8}
$$

$$
\approx 0.8 \times 10^2 \left(\frac{R_{\text{WD}}}{10^9 \text{cm}} \right) \left(\frac{M_{\text{BH}}}{10^3 M_\odot} \right)^{-2/3} \left(\frac{M_{\text{WD}}}{0.6 M_\odot} \right)^{-1/3} R_G \ ,
\tag{9}
$$

for a black hole mass M_{BH}, stellar radius R_{WD}, and stellar mass M_{WD}. R_G is a convenient scale length defined by the gravitational radius

$$
R_G = \frac{G M_{\text{BH}}}{c^2} \approx 1.5 \times 10^3 \frac{M_{\text{BH}}}{10^3 M_\odot} \text{km} \ .
\tag{10}
$$

Table 1. Run Parameters

Run	M_{BH} ($M_\odot$)	M_{WD} ($M_\odot$)	R_{WD} (R_G)	R_{P} (R_G)	R_{P}^* (R_G)	Spin (M_{BH})	Orbit	β	β^*
A9p-c	10^3	0.6	5.7	10	8.0	0.9	prograde	6.8	8.5
A9p-b	10^3	0.6	5.7	12.5	10.7	0.9	prograde	5.4	6.3
A0-b	10^3	0.6	5.7	13.5	10.6	0	-	5.0	6.4
A9r	10^3	0.6	5.7	15	10.8	0.9	retrograde	4.5	6.3
A0-a	10^3	0.6	5.7	15	12.3	0	-	4.5	5.5
A9p-a	10^3	0.6	5.7	15	13.3	0.9	prograde	4.5	5.1
A9m	10^3	0.6	5.7	15	12.3	0.9	polar	4.5	5.5
A9p-c	10^3	0.6	5.7	10	8.1	0.9	prograde	6.8	8.4
A9r	10^3	0.6	5.7	15	10.7	0.9	retrograde	4.5	6.3
A9p-a	10^3	0.6	5.7	15	13.4	0.9	prograde	4.5	5.1
B9p-b	10^4	0.15	1.1	7	6.3	0.9	prograde	6.3	7.0
B0-b	10^4	0.15	1.1	8	5.7	0	-	5.5	7.7
B9r	10^4	0.15	1.1	10	5.3	0.9	retrograde	4.4	8.3
B0-a	10^4	0.15	1.1	10	8.2	0	-	4.4	5.4
B9m	10^4	0.15	1.1	10	8.3	0.9	polar	4.4	5.3
B9p-a	10^4	0.15	1.1	10	9.3	0.9	prograde	4.4	4.7

Table 1 shows the different case studies considered in this report, focusing on five principle parameters: BH mass ($M_\odot$), WD mass ($M_\odot$), black hole spin (BH mass units), spin-orbit alignment, and interaction strength (β). Also shown are the star radii R_{WD}, the actual calculated (relativistically corrected) perihelion distance R_P^*, and the relativistically corrected tidal strength β^* experienced by the mass centroid of the WD in the simulations. The run labels represent physical parameters: The first (letter) index signifies the [BH, WD] mass combination (A$\equiv [10^3, 0.6]\ M_\odot$, B$\equiv [10^4, 0.15]\ M_\odot$), the second (number) index is the BH spin, and the third (letter) index identifies the orbit as retrograde, prograde, or polar (equivalently mid-plane alignment). The index following the hyphenation is simply a running letter index representing different perihelion radii and therefore different β. The order in which the cases are presented in Table 1 reflects the results shown later in Table 2: from highest peak temperature to lowest within each grouping.

The new physics elements incorporated into this work (Helmholtz EOS, particle tracers, self-gravity) come at significant computational cost. In order to perform all the calculations needed to cover the parameter space we are forced to carry out many of the calculations at less than ideal grid resolution, on a 96^3 grid with two in place of three AMR levels. The high resolution calculations are run on a 96^3 grid with three grid hierarchies and are identified with the same notation in Table 1 except they are highlighted in bold text. Although the grid resolution suffers by a factor of two in directions parallel to the orbital plane, our grid motion strategy preserves the vertical scale height resolution of 10^6 cm in the orbital plane at the expense of coarser zoning nearer grid boundaries.

Our choice of parameters is in part motivated by a compromise between proximity to the black hole in order to maximize tidal and spin effects, and the scale height resolution needed to adequately resolve nuclear processes in the orbital plane, a constraint that depends strongly on the tidal strength $\delta z/R_{\mathrm{WD}} \sim \beta^{-3}$ (Luminet & Carter 1986; Brassart & Luminet 2008), where δz is the grid resolution perpendicular to the orbital plane. This is the primary motivation for our selection of tidal strengths: they are large enough to trigger robust nucleosynthesis but not so large as to require excessive vertical resolution.

We point out that the (β, R_P) pairings quoted in Table 1 differ slightly from Paper 1. This is due to the different initial stellar models adopted for this work. In another final departure from our previous work, we do not rely on solutions to the relativistic Tolmon-Oppenheimer-Volkof (TOV) equations for the initial data. Instead, we use hydrodynamic

profiles generated from the MESA stellar evolution code (Paxton et al. 2011), including density, internal energy, and isotopic compositions. These profiles do not differ much (to within roughly a factor of two) from our older stellar models in density, radial extent, and temperature. They do however differ enough that the same perihelion radius does not produce the same tidal strength characterization (β) presented in our previous studies. Additionally the masses differ slightly as well. Although the 0.6 $M_\odot$ WD is very close to what we considered previously (to within a few percent), the equivalent $0.2M_\odot$ model is now more precisely a 0.15 $M_\odot$ WD. These are some of the reasons that we (re)consider nonrotating BH interactions in this work (the upgrade to a Helmholtz EOS is another).

As for isotopic compositions, the 0.6 $M_\odot$ model is composed of a central region with roughly a homogeneous mixture of 1/3 ^{12}C and 2/3 ^{16}O with trace amounts of heavier nuclei, surrounded in turn by layers of carbon-rich, helium-rich, and hydrogen-rich material, ordered from the inner core to the outer surface. The 0.15 $M_\odot$ model is composed of essentially a uniform distribution of 99% (by mass fraction) ^{4}He with trace amounts of other species. Considering the dominance of CO and He in the two stellar models, we occasionally refer the 0.6 (0.15) $M_\odot$ WD as CO (He) WD. MESA produces a much greater number of isotopes than appear in the inlined 19-isotope burn model. The integrated mass fractions of those species is small (less than 1 to 2 percent, depending on the He or CO WD) so we ignore them and renormalize the sum of mass fractions to unity with a density weighted scaling applied to each existing isotope.

3. RESULTS

The range of interaction strengths for case A encounters of a CO WD with a $10^3 M_\odot$ BH are within the upper bound ($\beta_S = 8.4$) where the BH swallows the WD (Kawana et al. 2018)

$$\beta_S \lesssim 10 \left(\frac{R_{\rm WD}}{10^9 \text{cm}} \right) \left(\frac{M_{\rm BH}}{10^3 M_\odot} \right)^{-2/3} \left(\frac{M_{\rm WD}}{0.6 M_\odot} \right)^{-1/3} . \tag{11}$$

Case B encounters, on the other hand, lie at or outside the margins of this limit ($\beta_S \approx 5.5$) so that if relativistic (or dissipative) effects drive the WD too far inward from the initial Keplerian trajectory, much of the tidal debris can be swallowed directly and leave little unbound material. However the parameter space associated with $10^4 M_\odot$ BHs that is also capable of giving rise to robust nucleosynthesis is extremely limited. So we consider this case only to gauge the effect of BH mass and tidal force gradient on the efficiency of nucleosynthesis, even if most of the debris is bound to or swallowed by the BH. For this reason we restrict calculations of this binary system to just two levels of refinement. A few of the more interesting case A scenarios are run at both two and three refinement levels to assess convergence.

These relatively moderate values of β conveniently place the perihelion radii of all spin-orbit orientations that we consider outside of the inner most stable circular orbit (ISCO) and the marginally bound orbit (MBO)

$$r_{\rm MB} = 2M \pm a + 2\sqrt{M(M \pm a)} , \tag{12}$$

where the + (-) sign applies to retrograde (prograde) orbits. The stars have radii smaller than the difference between perihelion and ISCO radii, suggesting that very little WD material will get swallowed by the BH prior to passing through periapsis, assuming the interaction strength is also sufficiently smaller than β_S. For reference, the (ISCO, MBO) radii evaluate to (2.3, 1.7) R_G for prograde and (8.7, 5.7) R_G for retrograde orbits around a BH with spin parameter $a = 0.9 M_{\rm BH}$. Of course these degenerate to (6, 4) R_G with zero spin.

Figure 1 shows color images of the logarithm of the ^{56}Ni, ^{40}Ca, and total (sum of all species) mass densities in the orbital plane for cases A9p-c and A9r at early and late times when the WD first approaches periapsis and as it ends its first clockwise pass around the black hole. Figure 2 shows the corresponding gas temperatures in units of Kelvin. These images exhibit typical behaviors found in all of our encounter scenarios: Calcium group elements begin to form the moment stellar matter compresses to maximum density in the orbital plane and heats to ignition temperatures, primarily along the radially aligned feature evident in the early (left) images of both the density and temperature figure sets. Shocks develop above and below the orbital plane, as shown in Figure 3, contributing to the ignition of nuclear fuel and thermal runaway conditions capable of burning through to iron. Burn products, after having formed in the central high density regions, follow in the wake of these shocks which move off the orbital plane at velocities between 0.03 to 0.09c. Heavier elements subsequently form within the confines of the lighter elements, giving rise to a layered structure resembling SN Ia models where the densest parts of the debris are composed mostly of iron products surrounded by intermediate mass elements, which in turn are embedded within an outer layer of unspent fuel. Once nucleosynthesis gets started, the composition of burn products is generally established fairly quickly, within a half second or so before stellar material decompresses.

Although highly resolved for three dimensions, our calculations do not cover fully the spatial range needed to determine precisely where the shocks emerge, or whether they are responsible for triggering or simply enhancing ignition. Instead we refer to the work of Tanikawa et al. (2017) who performed much more highly resolved 1D simulations down to scales of 10^4 cm, adopting dynamical flow conditions from 3D SPH models. Their calculations demonstrate a network of shocks develop within the scale height of stellar matter at different locations above and below the orbital plane. The forward-most shocks (which in the 3D calculations are delineated by the outer unit Mach number contour in the lower lobe of Figure 3) do not accompany sustained detonation waves; they decay due to propagating through low density fuel. Sustained detonations occur within a few hundred kilometers from the orbital plane (near the inner Mach number contour of Figure 3) and are powered by a combination of tidal compression and shocks so long as they break out at densities $\gtrsim 10^6$ g cm^{-3}. Their work additionally established a minimum resolution requirement for 3D calculations of $\lesssim 10^6$ cm in order to achieve reasonably converged solutions for triggering detonation and generating nuclear yields, a scale that we have intentionally matched in this work.

Our calculations suggest detonations may be triggered spontaneously, not by direct initiation. Although we cannot entirely rule out the latter possibility due to limited resolution, we find no evidence in the simulations that hydrodynamic shocks trigger ignition. Rather they appear to enhance developing hotspots and to facilitate thermonuclear burn after the fuel first ignites from induction gradients within the shock confined regions. In this scenario it is important to resolve the critical length scale needed to generate a detonation wave, which rapidly decreases with increasing fuel density. Tracing the origin of the initiation, we find pockets of burn products at the earliest stages of nucleosynthesis correlate with the highest density regions at the center of the WD. These regions host roughly two-to-one oxygen/carbon ratios at mean densities $\sim 10^7$ g cm^{-3} and temperatures between $2 - 2.5 \times 10^9$ K, slightly less dense and cooler than their peak values at maximum compression. For such conditions Table 11 from Seitenzahl et al. (2009) predicts a minimum critical length scale of about 50 km, a number that they estimate is likely a factor of two or three low based on their resolution studies and well above our 10 km cell size.

3.1. *Inline Nucleosynthesis*

Table 2 summarizes our results at both high and low grid resolutions. Displayed are the actual (relativistically corrected) tidal strength, maximum densities, maximum temperatures, global nuclear energy production, and final (plateau) calcium and iron-group masses. We define iron group as those elements with atomic numbers in the range 52-60, calcium group between 40-51, and silicon between 28-39. For the 19-isotope inline network these group elements consist simply of (Fe, Ni), (Ca, Ti, Cr), and (Si, S, Ar), respectively.

There is generally good agreement in the density/temperature phase tracks between low and high resolution cases: temperatures match to roughly 20%, and the densities to about a factor of two, suggesting that we have come close to converging on the mid-plane compression, but not quite. These differences manifest as 30% uncertainty in the total nuclear energy released, and about a factor of two in burn product synthesis.

It is not surprising to find some sensitivity of our results to grid resolution since the critical length scales for carbon and helium burn are small and difficult to achieve in three dimensional calculations (Seitenzahl et al. 2009; Holcomb et al. 2013). However it is encouraging that our results are not strongly dependent on resolution, as would be the case if they are entirely due to poor resolution. As noted earlier, we attribute this to matching the grid scale conditions ($\lesssim 10^6$ cm) suggested by the 1D studies carried out by Tanikawa et al. (2017) for establishing converged solutions at the interaction strengths considered in this work.

Comparing the two nonrotating cases A0-a and B0-a to the nearest equivalent cases in Paper 1 we can additionally assess effects from all the physics upgrades incorporated into these new studies, namely the MESA (as opposed to TOV) generated stellar models, the Helmholtz EOS, and dynamic self-gravity. Because of the different stellar models, there is no exact encounter scenario to which we can directly compare results. However we point out that case A0-a is close in interaction strength to B3M6R12 from Paper 1, but closer to B3M6R9 in perihelion approach to the BH. Comparing our current results to both of these cases we find generally good agreement in the peak density, peak temperature, total nuclear energy and calcium production, roughly an average factor of two in all these diagnostics. Iron production differs the most, but our current results lie between these two cases which happen to straddle the parameter space in a region of strong sensitivity.

The nonrotating case B0-a has an interaction strength and perihelion radius slightly greater than but comparable to B4M2R6 from Paper 1. These two cases similarly agree quite well in peak density and temperature (about a factor of 2), energy released (10%), and small or negligible levels of both calcium and iron group elements. Our previous results
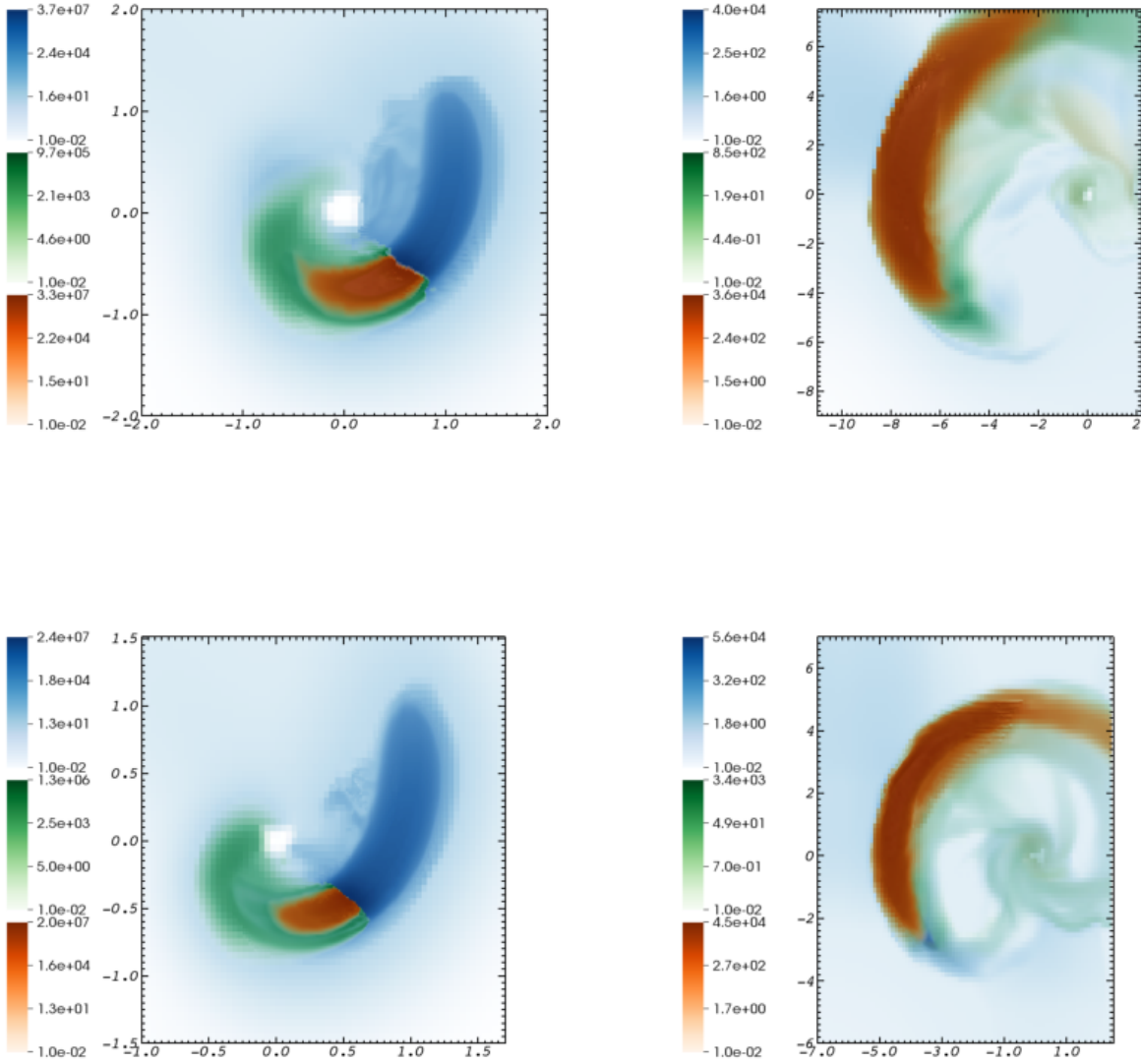
Figure 1. Logarithm of the ^{56}Ni (orange color map), ^{40}Ca (green color map), and total mass densities (blue color map) sliced through the orbital plane for case A9p-c at times 0.04 (top left) and 2 secs (top right), and for case A9r at 0.02 (bottom left) and 2 secs (bottom right). Legends are densities in g cm^{-3}. Spatial scales are in units of R_P.

presented in Paper 1 are thus validated to roughly a factor of 2 collectively, despite using less sophisticated physical models.

Quantifying nuclear activity by both the nuclear energy released and mass conversion efficiency to iron products, we find that rotation effects from $10^3 M_\odot$ BH encounters is quite small. Adjusting the perihelion radius to produce comparable $\beta^* \approx 5.5$ interaction strengths, nuclear activity varies by only 25% comparing cases A0-a (no rotation), A9m ($a = 0.9$, polar orbit), and A9p-a ($a = 0.9$, prograde orbit). A similarly small variation is observed comparing $\beta^* \approx 6$ encounters with a $10^3 M_\odot$ BH (cases A0-b, A9r, and A9p-b), and $\beta^* \approx 8$ encounters with a $10^4 M_\odot$ BH (cases B0-b, B9r, and B9p-b), regardless of whether the BH is rotating or not, or whether the spin-orbital vectors are aligned or not. These comparisons are evaluated at the relativistic (not Newtonian) penetration factors β^* and thus account for the actual tidal strength experienced by the stellar mass centroids in each of the models, which depends
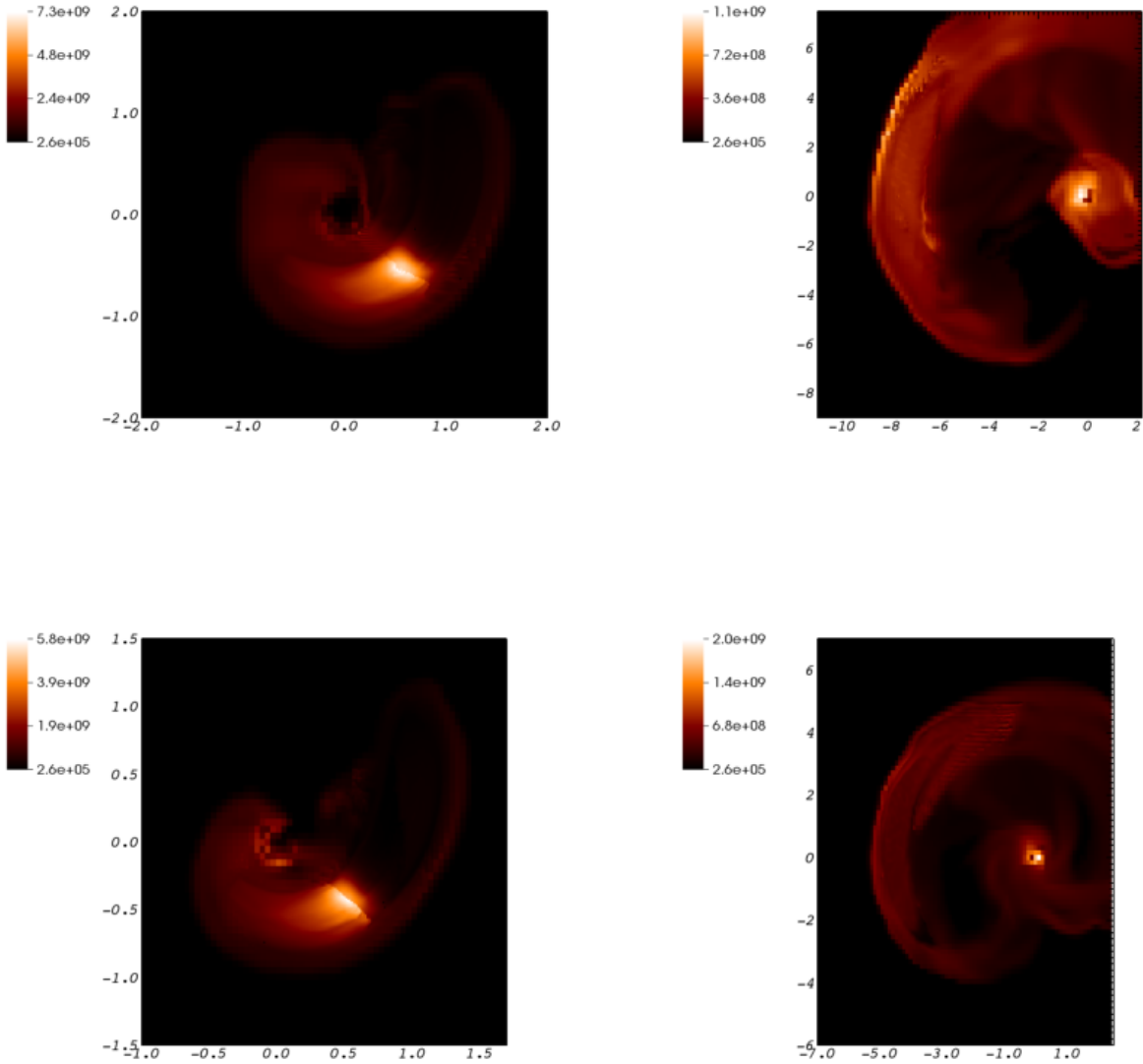
Figure 2. Gas temperature in units of Kelvin corresponding to the image sequences of Figure 1.

rather sensitively on BH spin alignment: retrograde (prograde) orbits approach closer to (further from) the BH than the Keplerian approximation would predict due to the loss (gain) of angular momentum from frame dragging effects. Whether this small difference is physical or numerical is difficult to say: as we have noted above, 25% variance in nuclear energy is roughly the level of numerical uncertainty at our current grid resolution.

3.2. *Post-processed Nucleosynthesis*

At the start of each calculation, stellar interiors are sampled with approximately fifteen-thousand particles that are evolved (passively advected) in time according to their Lagrangian velocity using a second order predictor-corrector scheme. The initial angular distribution of particles inside the white dwarf is random but isotropic. Radial positions are randomly sampled from a mass distribution function derived by inverting the MESA generated mass-radius profiles, which produces a nearly uniform mass for all particles and concentrates particles towards the core center in a way
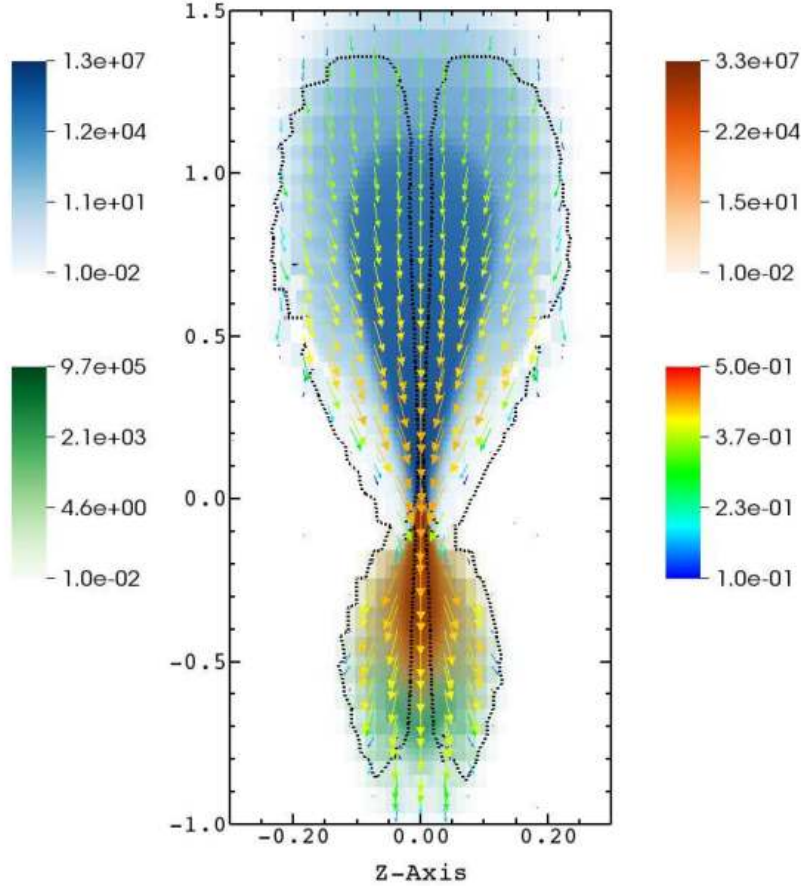
Figure 3. Logarithm of the ^{56}Ni (orange color map), ^{40}Ca (green), and ^{12}C mass densities (blue) sliced through the center of the hotspot developing in Figure 1 in a plane orthogonal to the line directed towards the black hole. The image corresponds to case A9p-c at 0.04 secs, the same time as the left image of Figure 1. Vectors (rainbow map) track the fluid motion compressing towards the $z = 0$ orbital plane (top lobe), then decompressing supersonically (bottom lobe) after bouncing off the mid-plane. The dotted black line is the contour surface where the Mach number of the z-velocity component is unity. Densities are in g cm^{-3}, velocities are scaled to the speed of light, and axes labels are in units of R_P.

that respects the stellar density profile. All particles are endowed with physical attributes (e.g., temperature, density, and energy density) that are interpolated using an inverse covariant distance weighting scheme contributed to by nearest (shared face) neighbor cells and projected to particle positions. Particle positions and thermodynamic states are computed each cycle as part of the hydrodynamic update sequence, but are stored to disk at less regular intervals in preparation for post-processing with a more elaborate 495-isotope nuclear reaction network adapted from the Torch code (Timmes 1999). Particles falling into the BH horizon are discarded and thus ignored in the final analysis. This treatment improves on the post-processing method of Paper 1 by sampling the entire star (not just the inner dense core), and by tracking the stellar interior along Lagrangian fluid elements (not just within the densest Eulerian cells).

The specific energy spread associated with tidal forces is approximated to within a numerical constant of order unity as (Stone et al. 2013; Kawana et al. 2018)

$$\Delta\epsilon_{\rm tidal} \approx \frac{GM_{\rm BH}R_{\rm WD}}{R_T^2} \approx 1.2\times10^{-3}c^2\left(\frac{R_{\rm WD}}{10^9{\rm cm}}\right)^{-1}\left(\frac{M_{\rm BH}}{10^3M_\odot}\right)^{1/3}\left(\frac{M_{\rm WD}}{0.6M_\odot}\right)^{2/3}. \tag{13}$$

Considering lower mass stars also have larger radii, two of the three binary system parameters in equation (13) conspire to produce smaller energy spreads for the B-series calculations. Additionally, the relatively inefficient nuclear energy

Table 2. Inline Result Summary

Run	β^*	$\rho_{\max}$ (g cm^{-3})	$T_{\max}$ (K)	e_{nuc} (erg)	$M_{\mathrm{Fe,max}}$ ($M_\odot$)	$M_{\mathrm{Ca,max}}$ ($M_\odot$)
A9p-c	8.5	2.0×10^7	5.6×10^9	7.5×10^{50}	2.7×10^{-1}	2.1×10^{-2}
A9p-b	6.3	1.8×10^7	4.8×10^9	6.2×10^{50}	1.2×10^{-1}	1.4×10^{-2}
A0-b	6.4	1.7×10^7	4.6×10^9	5.8×10^{50}	8.8×10^{-2}	1.6×10^{-2}
A9r	6.3	1.8×10^7	4.5×10^9	5.8×10^{50}	9.1×10^{-2}	1.5×10^{-2}
A0-a	5.5	1.6×10^7	4.2×10^9	4.9×10^{50}	4.4×10^{-2}	1.0×10^{-2}
A9p-a	5.1	1.6×10^7	4.0×10^9	4.4×10^{50}	3.3×10^{-2}	8.0×10^{-3}
A9m	5.5	1.2×10^7	3.9×10^9	4.6×10^{50}	3.5×10^{-2}	7.5×10^{-3}
A9p-c	8.4	4.6×10^7	6.8×10^9	8.3×10^{50}	4.0×10^{-1}	1.8×10^{-2}
A9r	6.3	3.5×10^7	5.3×10^9	7.3×10^{50}	2.1×10^{-1}	2.3×10^{-2}
A9p-a	5.1	2.8×10^7	4.6×10^9	6.0×10^{50}	9.0×10^{-2}	2.1×10^{-2}
B9p-b	7.0	5.0×10^5	1.5×10^9	6.1×10^{49}	1.3×10^{-4}	1.1×10^{-2}
B0-b	7.7	5.3×10^5	1.4×10^9	5.5×10^{49}	9.3×10^{-5}	9.1×10^{-3}
B9r	8.3	5.9×10^5	1.0×10^9	3.2×10^{49}	1.4×10^{-5}	4.3×10^{-3}
B0-a	5.4	5.0×10^5	7.1×10^8	6.3×10^{48}	$< 10^{-15}$	5.0×10^{-12}
B9m	5.3	3.3×10^5	5.4×10^8	2.5×10^{48}	$< 10^{-15}$	$< 10^{-15}$
B9p-a	4.7	4.5×10^5	4.1×10^8	3.4×10^{47}	$< 10^{-15}$	$< 10^{-15}$

released (in Table 2) from this class B encounter scenario suggests that the effect of nuclear reactions on debris motion is small since $\Delta\epsilon_{\mathrm{tidal}} > \Delta\epsilon_{\mathrm{nuc}}$, where $\Delta\epsilon_{\mathrm{nuc}} \approx 10^{49}\mathrm{erg}/M_{\mathrm{WD}} \approx 10^{-4}c^2$. Hence in this section we consider only the A-series calculations where nuclear energy release is expected to be more important.

Table 3 summarizes the total nuclear energy released, along with the peak calcium ($M_{\mathrm{Ca,max}}$) and iron ($M_{\mathrm{Fe,max}}$) masses produced in each calculation, which should be compared (and be comparable) to the corresponding results in Table 2 calculated with the inline 19-isotope model. Looking especially at the high resolution calculations, we find the 19 and 495 isotope models agree remarkably well; roughly 20% on the plateau (final) total energy release and calcium production, and within 75% on the amount of iron. The production histories of Fe, Ca, and Si group elements are plotted in Figure 4 for the high resolution cases A9p-c, A9r, and A9p-a. Solid (dotted) lines represent results from the inline 19 (post-processed 495) isotope network models. Apart from the relative amounts of Fe, Ca, and Si produced, which transitions from Fe dominated to Si dominated with increasing perihelion radius, these results are typical in that the more accurate 495 isotope model predicts slightly greater intermediate element production at the expense of iron. Agreement between the simple and complex models is otherwise excellent for all group elements and throughout time.

Also shown in Table 3 is the total unbound mass ($M_{\mathrm{tot,unbnd}}$) and the unbound mass of burn products ($M_{\mathrm{Fe,unbnd}}$, $M_{\mathrm{Ca,unbnd}}$) estimated by summing up the mass of all particles found with positive specific orbital energy ($\epsilon = v^2/2 - GM/r$) at the final simulation time of 2 seconds past periapsis. At interaction strength $\beta^* \approx 5.5$ (runs A0-a, A9m, and A9p-a), the average mass conversion efficiency of total (bound plus unbound) iron and calcium is roughly the same, 3-5%, with a very weak (if any) dependence on BH spin. About 40-50% of all iron and 30-40% of all the calcium produced is unbound in these cases, regardless of BH spin.

Prograde orbital alignment allows for the WD companion to approach closer to the BH without falling inside the ISCO (or MBO), offering the intriguing possibility of producing more unbound intermediate and heavy elements. As expected, we do observe significantly greater iron production at smaller perihelion radii (compare cases A9p-a, A9p-b, and A9p-c, where the latter case reduces the perihelion radius to the minimum value before the outer layers of WD material hit the ISCO). However the capture cross-section increases as well and we find a somewhat smaller, but still an order of magnitude increase, in the amount of unbound iron group elements. The total (unbound) mass conversion
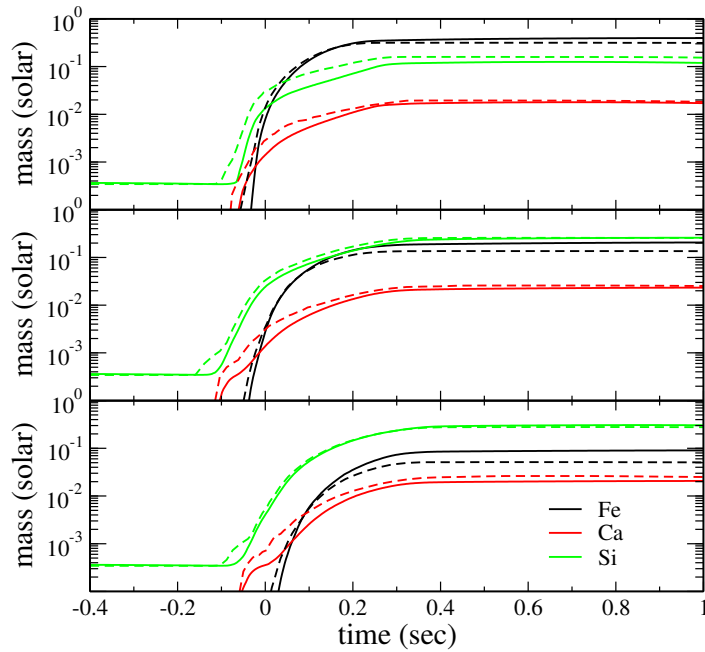
Figure 4. Production and evolution of Fe, Ca, and Si group elements from the high resolution cases: A9p-c (top), A9r (middle), and A9p-a (bottom). Solid (dotted) lines represent results from the 19 (495) isotope network model.

efficiency for these scenarios peaks at about 50% (70%) in the high resolution case A9p-c. Roughly 50-60% of all iron and 35-40% of all calcium group elements are unbound in both the more distant (A9p-a) and closer (A9p-c) cases, though the latter produces an order of magnitude more unbound and total iron mass. Furthermore, whereas the fraction of unbound iron increases with decreasing perihelion radius, the fraction of unbound calcium remains nearly constant, suggesting (as we demonstrated in Paper 1) that the ratio of unbound intermediate to heavy group elements might prove to be a defining signature of binary system parameters. Comparing cases A9p-a and A9p-c where the perihelion radius is reduced by about 1/3, the ratio of unbound calcium to unbound iron mass is reduced by an order of magnitude.

By way of validation, we point out that our results concerning the amount of unbound debris are generally consistent with those published by Kawana et al. (2018) for the case of nonrotating BHs. We additionally note that the rotating BH case A9p-c evolves to a comparable penetration factor as run B6Su in Haas et al. (2012), and results in a nearly identical total unbound mass fraction, 50% compared to 60%.

3.3. *Spatial Distribution*

All calculations are terminated shortly after nucleosynthesis settles to small fractional energy changes, no longer than 2 seconds after reaching periapsis. Hence we do not (in this work) follow fall-back effects. Instead we approximate the distribution and composition of bound versus unbound debris by calculating the specific orbital energy of each

Table 3. Post-processed Result Summary

Run	β^*	e_{nuc}	$M_{\mathrm{tot,unbnd}}$	$M_{\mathrm{Fe,max}}$	$M_{\mathrm{Fe,unbnd}}$	$M_{\mathrm{Ca,max}}$	$M_{\mathrm{Ca,unbnd}}$
		(erg)	$(M_\odot)$	$(M_\odot)$	$(M_\odot)$	$(M_\odot)$	$(M_\odot)$
A9p-c	8.5	7.5×10^{50}	3.0×10^{-1}	2.5×10^{-1}	1.3×10^{-1}	2.4×10^{-2}	1.1×10^{-2}
A9p-b	6.3	6.4×10^{50}	3.0×10^{-1}	1.0×10^{-1}	6.1×10^{-2}	3.0×10^{-2}	1.3×10^{-2}
A0-b	6.4	6.1×10^{50}	2.8×10^{-1}	7.2×10^{-2}	3.7×10^{-2}	2.8×10^{-2}	1.0×10^{-2}
A9r	6.3	5.8×10^{50}	3.0×10^{-1}	6.2×10^{-2}	3.6×10^{-2}	2.6×10^{-2}	1.1×10^{-2}
A0-a	5.5	5.1×10^{50}	2.7×10^{-1}	2.5×10^{-2}	1.3×10^{-2}	2.3×10^{-2}	8.2×10^{-3}
A9p-a	5.1	4.7×10^{50}	2.9×10^{-1}	1.8×10^{-2}	1.2×10^{-2}	2.0×10^{-2}	8.1×10^{-3}
A9m	5.5	5.1×10^{50}	3.2×10^{-1}	3.0×10^{-2}	1.7×10^{-2}	2.2×10^{-2}	1.0×10^{-2}
A9p-c	8.4	7.1×10^{50}	3.0×10^{-1}	3.2×10^{-1}	2.0×10^{-1}	1.9×10^{-2}	7.4×10^{-3}
A9r	6.3	6.0×10^{50}	2.7×10^{-1}	1.4×10^{-1}	8.4×10^{-2}	2.6×10^{-2}	1.1×10^{-2}
A9p-a	5.1	5.0×10^{50}	2.6×10^{-1}	5.1×10^{-2}	3.4×10^{-2}	2.6×10^{-2}	1.1×10^{-2}

particle tracer at the end of the simulations, then assume bound particles with negative orbital energy subsequently evolve in a collisionless fashion after having settled onto closed Keplerian orbits. This allows us to approximate the late-time radial extent of the debris distribution as $R_{\mathrm{max}} = -GM/(2\epsilon)$, where R_{max} is effectively the semi-major axis of the (closed) orbital trajectories.

In this way we find the radial distribution of nuclear burn products does not vary much. For example, the mass of nuclear debris (when catalogued into Fe, Ca and Si groups) trapped within $R_{\mathrm{max}} < 10R_G$ is generally only about twice the corresponding group amount traveling on unbound trajectories. As shown in Figure 5, the ratio of burn products when normalized to total iron content is just as evenly distributed, varying by less than a factor of two across many orders of magnitude in radius. For each case we have considered (A9p-a, A9p-c, A9r), the ratio of unbound intermediate mass elements relative to iron is less than what can be found in bound debris (by a factor of two), and a clear transition between near and far field distributions occurs in all calculations between 100 and 200 R_G.

The seemingly uniform logarithmic shifts between each of the three cases plotted in Figure 5 suggests that perhaps a simple scaling law can be useful for approximating species mass fractions. For example, applying a least squares fit to a generic polynomial of the form $M_F \propto (\beta^*)^{-n}$, the mass ratios can be fit in both the near and far fields rather nicely by exponents $n \sim (4.3,\ 4.8)$ for the (Ca/Fe, Si/Fe) ratios respectively. The polynomial fits are performed at two different radii, 50 and 900 R_G, and represented as symbols in Figure 5: circles for Ca/Fe, crosses for Si/Fe. Of course the range of parameter space used in determining these fits is rather limited, so we cannot reliably extrapolate this scaling beyond the intermediate tidal strength interactions ($5 \lesssim \beta^* \lesssim 9$) studied in this report.

3.4. *Isotopic Distribution*

Table 4 presents the final isotopic mass fractions of the dominant stable species for both the unbound and total (bound plus unbound) stellar matter that survived to the end of the high-resolution runs A9p-a, A9r, and A9p-c. The fraction of unbound material in these three runs sum to 43, 45, and 50% of the total mass respectively. In the second and third columns we list the element that contained the most mass in the decay chain leading to the stable species shown (i.e. their radioactive progenitors), and their corresponding mass fractions in the Sun (Lodders 2003).

All species shown are produced as self conjugate (Z=N) alpha nuclei. Since our initial compositions are mixtures of alpha particles, essentially ^{4}He, ^{12}C, and ^{16}O (see Figure 1 in Paper 1), there is no initial neutron excess, and subsequently minimal production of more neutron rich species. As the peak temperature increases in ever closer encounters (progressively in the order A9p-a, A9r, Ap9-c) heavier species are produced with an ever larger fraction of the final mass ending up in ^{56}Ni.

From the ensemble of tracer particles in runs A9p-a, A9r, and A9p-c we can easily identify and extract individual thermodynamic trajectories favorable to the production of any specified isotope. We find, for example, that trajectories winding up with large mass fractions of ^{48}Cr (^{56}Ni) originate from the outer (inner) portions of the WD, > 5000
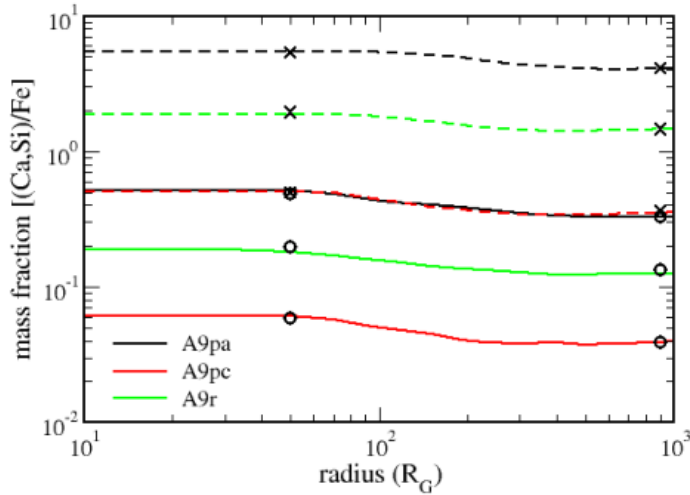
Figure 5. Approximate late-time mass fractions of intermediate mass elements relative to iron are plotted as a function of radius from the BH in R_G units. Solid (dotted) lines represent Ca/Fe (Si/Fe) mass fractions. The different colors correspond to the three different cases A9p-a (black), A9p-c (red), and A9r (green). Circles (crosses) are polynomial fits to the Ca/Fe (Si/Fe) fractions at 50 and 900 R_G.

(< 1000) km from the center core. The initial compositions of these trajectories consist of roughly 70/30 ratios of ^{4}He/^{12}C (^{16}O/^{12}C) for the ^{48}Cr (^{56}Ni) producing tracks. Because of the high densities and relatively long burning times, the production of Ca, Ti, and Cr resembles explosive helium burning (Woosley 1986) taking place in the outer regions of the WD. The high densities also allow for efficient conversion of alpha-particles to carbon, resulting in final alpha-particle mass fractions that were small (less than a few percent) in all scenarios studied here. Because of the much higher temperatures ($> 5 \times 10^9$ K) experienced by material closer to the center of the WD, the heavier products (Fe, Co, Ni, Zn) created under these conditions resemble material that reached nuclear statistical equilibrium at zero neutron excess (Hartmann et al. 1985). ^{64}Zn (made here as ^{64}Ge) is at the end of the production chain since proton-unbound species above it prevent further synthesis in the absence of robust neutrino emission (Pruet et al. 2006; Fröhlich et. al. 2006).

Several species observed in our calculations are of interest because they contain gamma-ray emitting nuclei in their decay pathways. The gamma-ray and positron energy from decay of these species, especially ^{56}Ni and ^{56}Co, is converted into kinetic energy of the debris or thermalized with most of the flux appearing at optical wavelengths Suntzeff (2002). While we anticipate that tidal encounters will most likely be first observed through photometric means, we do point out that with very little to no envelope material surrounding the white dwarf, and the tidal forces acting to produce a spray rather than an expanding photo-sphere, that the gamma-ray diffision times may be short, thus giving rise to the possibility of gamma-ray line emission from some of these species that might be observable. We provide below a short discussion of the prominant gamma-lines and develop approximate bolometric light curves in the next section.

^{44}Ti, with a half-life of 60 years, decays through ^{44}Sc to ^{44}Ca. The dominant (99.88% per ^{44}Sc decay) gamma-line observed in Type II supernova remnants is the 1157 keV from the 2+ excited state to the 0+ ground state in ^{44}Ca, although the 78.36 and 67.86 keV lines from the 0- and 1- states in ^{44}Sc have also been observed (Timmes et al. 1996; Hoffman et al. 2010). Because of the uncertainty in the crucial production and destruction reaction rates affecting its synthesis (we use the theoretical rates from Rauscher & Thielemann (2000)), our calculated results for ^{44}Ti synthesis may well be uncertain by a factor of two or more (Hoffman et al. 2010).

Table 4. Final Composition Summary

Nucleus	Progenitor	$X_\odot$ (solar)	$X_{\rm tot}$ (A9p-a)	$X_{\rm tot}$ (A9r)	$X_{\rm tot}$ (A9p-c)	$X_{\rm unb}$ (A9p-a)	$X_{\rm unb}$ (A9r)	$X_{\rm unb}$ (A9p-c)
^{4}He	He	2.74×10^{-1}	1.22×10^{-2}	1.14×10^{-2}	3.77×10^{-2}	8.15×10^{-3}	5.84×10^{-3}	3.68×10^{-2}
^{12}C	C	2.46×10^{-3}	8.08×10^{-2}	2.95×10^{-2}	4.23×10^{-4}	9.22×10^{-2}	3.74×10^{-2}	1.61×10^{-4}
^{16}O	O	6.60×10^{-3}	2.02×10^{-1}	1.40×10^{-1}	4.85×10^{-2}	1.78×10^{-1}	1.21×10^{-1}	4.59×10^{-2}
^{24}Mg	Mg	5.65×10^{-4}	2.33×10^{-2}	2.04×10^{-2}	7.62×10^{-3}	1.61×10^{-2}	1.57×10^{-2}	7.52×10^{-3}
^{28}Si	Si	7.55×10^{-4}	3.06×10^{-1}	2.81×10^{-1}	1.54×10^{-1}	3.06×10^{-1}	2.70×10^{-1}	1.39×10^{-1}
^{32}S	S	3.96×10^{-4}	1.70×10^{-1}	1.56×10^{-1}	8.36×10^{-2}	1.78×10^{-1}	1.56×10^{-1}	7.40×10^{-2}
^{36}Ar	Ar	9.13×10^{-5}	3.99×10^{-2}	3.83×10^{-2}	2.00×10^{-2}	4.19×10^{-2}	3.78×10^{-2}	1.73×10^{-2}
^{40}Ca	Ca	7.13×10^{-5}	4.07×10^{-2}	3.93×10^{-2}	2.35×10^{-2}	4.05×10^{-2}	3.75×10^{-2}	1.98×10^{-2}
^{44}Ca	Ti	1.69×10^{-6}	1.13×10^{-3}	7.73×10^{-4}	9.00×10^{-4}	4.96×10^{-4}	3.28×10^{-4}	6.52×10^{-4}
^{48}Ti	Cr	2.51×10^{-6}	2.71×10^{-3}	3.83×10^{-3}	4.42×10^{-3}	1.20×10^{-3}	1.62×10^{-3}	3.81×10^{-3}
^{52}Cr	Fe	1.64×10^{-5}	9.29×10^{-3}	1.57×10^{-2}	1.34×10^{-2}	1.00×10^{-2}	1.49×10^{-2}	1.20×10^{-2}
^{56}Fe	Ni	1.26×10^{-3}	9.51×10^{-2}	2.47×10^{-1}	5.63×10^{-1}	1.16×10^{-1}	2.89×10^{-1}	5.97×10^{-1}
^{57}Fe	Ni	2.96×10^{-5}	9.79×10^{-4}	2.55×10^{-3}	9.28×10^{-3}	1.04×10^{-3}	2.67×10^{-3}	9.74×10^{-3}
^{59}Co	Cu	4.01×10^{-6}	2.22×10^{-6}	3.76×10^{-4}	3.26×10^{-3}	1.66×10^{-6}	4.25×10^{-4}	3.40×10^{-3}
^{60}Ni	Zn	2.20×10^{-5}	7.94×10^{-6}	1.10×10^{-3}	2.09×10^{-2}	4.54×10^{-6}	1.29×10^{-3}	2.40×10^{-2}
^{64}Zn	Ge	1.12×10^{-6}	9.92×10^{-9}	2.62×10^{-5}	9.25×10^{-4}	6.34×10^{-13}	3.03×10^{-5}	1.03×10^{-3}

^{48}Cr decays to ^{48}Ti through ^{48}V which has a half-life of 16 days. The dominant gamma lines (983.5 and 1312 keV) observed in this decay chain arise via strong E2 transitions in the ground state band of ^{48}Ti.

^{52}Fe decays to ^{52}Cr through ^{52}Mn with a 5.6 day half-life. 91.4% of the time the 6+ ground state of ^{52}Mn decays to the 6+ excited state in ^{52}Cr, and again strong E2 transitions in the ground state band give rise to the most intense gamma lines with energies of 1434, 935.5, and 744.2 keV.

The closest approach scenario (case A9p-c) is an interesting example of an encounter producing copius amounts of the iron group elements Fe, Co, and Ni along with the rarely seen ^{64}Zn. Again, each of these species are made as self-conjugate radioactive progenitors. Prominent gamma-ray lines from the decay of ^{56}Ni exhibit energies of 0.847 and 1.238, while those from decay of ^{57}Ni have energies of 0.122, 0.014, and 0.136 MeV.

^{59}Co is produced here as ^{59}Cu which decays through the long lived (76000 y) ^{59}Ni, but we would not expect any discernable gamma-rays (the Cu lifetime is very short with 60% decaying directly to the ground state of ^{59}Ni). The lifetimes of the species that decay to Ni and Zn are also too short to be considered as viable candidates for observation.

Our results suggest a number of radioactive species with potentially observable gamma lines are made in white dwarf tidal disruption events, and that specific lines and relative line strengths may effectively characterize the encounters. The collective imaging of ^{56}Ni, ^{57}Ni, and possibly ^{44}Ti, ^{48}V, ^{52}Mn (if made in sufficient quantities) would provide a fairly discriminating diagnostic of interaction strength.

3.5. *Luminosities*

In this section we apply simple models to estimate transient luminosities based on unbound ^{56}Ni yields calculated by multiplying the mass fractions in Table 4 with the total unbound masses in Table 3. The yields for the three high resolution cases A9p-c, A9r, and A9p-a are 0.179, 0.078, and 0.030 solar masses respectively. Figure 6 plots the ^{56}Ni yields against some of the other species produced in Table 4.

Clearly ^{56}Ni dominates the yields of the other radioactive species in all three encounter scenarios, typically by an order of magnitude or more. In the following we assume that the peak bolometric luminosity is due to energy deposition by the decay of ^{56}Ni and ^{56}Co (Arnett 1979), and adopt the procedure described in Dado & Dar (2015) to calculate light curves based on four model parameters: the ^{56}Ni yield (M_{56}), the rise time (t_r), a time scale for gamma-ray
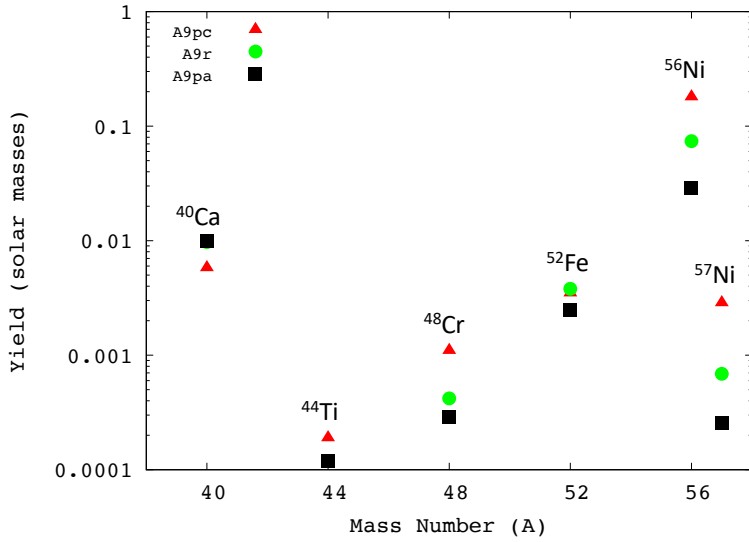
Figure 6. Unbound yields in solar mass units of ^{40}Ca together with the most abundant radioactive isotopes produced in cases A9p-c (red triangles), A9r (green circles), and A9-a (black squares).

Table 5. Parameters for light curve fits

Object	$M(^{56}\text{Ni})$	V_0	t_r	t_γ	t_{peak}	$\log(L_p)$	Δm_{15}^{bol}
	$(M_\odot)$	(c)	(d)	(d)	(d)	(erg s^{-1})	(mag)
SN 1992bc	0.840	0.050	12.60	26.80	17.50	43.19	0.93
SN 1991bg	0.110	-	-	-	-	42.32	1.42
A9p-c	0.179	0.039	8.03	27.31	13.50	42.68	0.88
		0.060	6.50	17.91	10.52	42.73	1.32
		0.090	5.31	11.94	8.52	42.75	1.84
A9r	0.078	0.037	8.29	29.12	13.52	42.31	0.79
		0.060	6.50	17.91	10.52	42.37	1.32
A9p-a	0.030	0.033	8.70	32.13	14.53	41.88	0.72
		0.060	6.50	17.91	10.52	41.95	1.32

energy deposition (t_γ), and the fraction of the energy released into the expanding fireball by positrons from the decay of ^{56}Co (A_e). These parameters in turn depend on the critical mass for the WD (M_C which we set to 0.6 $M_\odot$), our calculated ^{56}Ni yields, and an initial velocity for the fireball expansion (V_0).

Table 5 shows the inputs and derived quantites for the three high-resolution runs A9p-c, A9r, and A9p-a. From these runs we observed a range of expansion velocities ($0.03c \le V_0 \le 0.09c$). The lower limit is consistent with the assumption that the kinetic energy in the fireball is approximated by the total nuclear energy generated ($V_0 = \sqrt{2e_{nuc}/M_C}$). We also include the fitted parameters for SN 1992bc (V_0 0.05c, or 15,600 km s^{-1} Dado & Dar 2015).

In Figure 7 we show our calculated light curves for the three high resolution simulations together with experimental values of the bolometric luminosity for the branch-normal SN1992bc and the sub-luminous SN1991bg from Contardo et al. (2000). The top figure plots a series of light curves for A9p-c assuming a range of matter velocities (0.03c - 0.09c). This variation mostly affects rise and width of the light curves with a small change in peak luminosity that
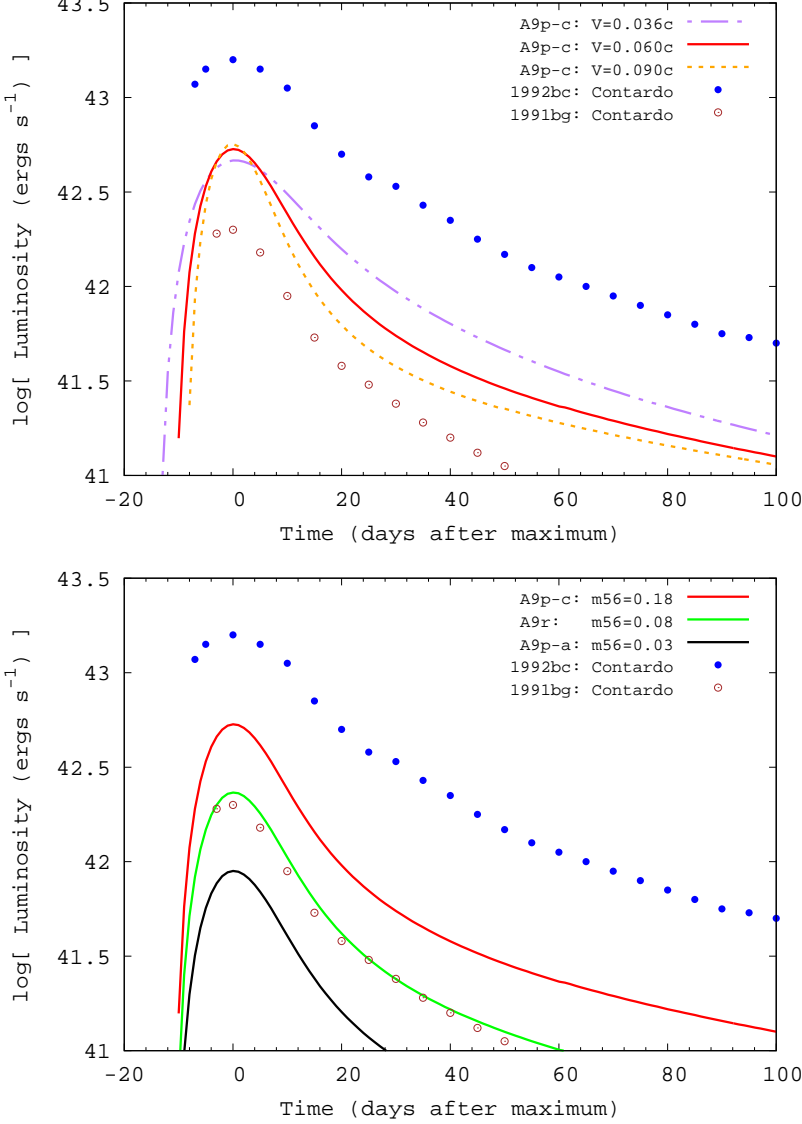
Figure 7. Light curves for case A9p-c over a range of expansion velocities V_0 (top), and cases A9p-c, A9r, and A9p-a assuming an average velocity of $0.06c$ (bottom). Also shown for comparison are the lightcurves from SN 1992bc and SN 1991bg.

favors the higher velocities. The value of A_e also affects the late time behavior, here we have taken a uniform value of 0.15 for all fits.

The bottom figure shows the light curve fits for Ap9-c, A9r, and A9p-a assuming an averaged expansion velocity for each of $0.06c$. The differences in peak luminosity arise from the calculated ^{56}Ni mass. Interestingly, the ^{56}Ni mass scales roughly linearly with interaction parameter β^* over the range of encounters considered here so that $L_b \propto M(^{56}Ni) \propto \beta^*$. Hence we can expect proportionally greater luminosities from prograde orbits whose characteristically smaller ISCO and MBO constraining radii allow closer encounters and thus greater interaction strengths.

Figures 7 demonstrate our simulated events are clearly sub-luminous compared to standard supernovae. The 15 day decline rates ($\Delta m_{15} \approx 2.5 \log[L_b(t_p)/L_b(t_p + 15d)]$) posted in Table 5, although highly sensitive to the expansion velocity parameter, are generally consistent with standard SN Ia data. The combination of lower luminosity but comparable decline rates aligns these tidal scenarios closer to SN 1991bg and SN type Iax events. We stress however that this analysis is over-simplified and perhaps not entirely appropriate to tidal encounters, especially considering the anisotropic nature of these events. We defer more accurate photometric and spectral processing to future work,

but note here that luminosities are expected to be strong functions of viewing angle and may vary by an order of magnitude or more (MacLeod et al. 2016).

4. CONCLUSIONS

We continue to develop and apply a novel numerical methodology to the tidal disruption of white dwarf stars from near encounters with intermediate mass black holes. Here as in Paper 1, we solve the general relativistic hydrodynamics equations in a Kerr-Schild spacetime to account for relativistic tidal forces, and utilize a hybrid AMR/moving mesh strategy to move the base grid along Lagrangian fluid lines while also refining down to a scale of $\sim 10^6$ cm on the densest parts of the white dwarf as it compresses and responds to tidal forces. This paper improves on our previous efforts by incorporating a tabular Helmholtz equation of state with electron degeneracy, significantly upgrading the original idealized 2-component model. We have also added a particle tracer capability for sampling and tracking stellar material along Lagrangian fluid lines, modified the Kerr-Schild metric to include a binding potential of the white dwarf solved dynamically each cycle, and adopted initial composition profiles from the MESA stellar evolution code in place of solving the hydrostatic Tolmon-Oppenheimer-Volkof (TOV) equations with a simplified equation of state model. As a result of these upgrades, although the primary objective of this paper is to extend previous work to include encounters with rotating and tilted black holes, we have also taken this opportunity to revisit a couple of the nonrotating BH encounter scenarios reported in Paper 1.

As a consequence of using MESA (not TOV) generated initial stellar models, slight differences in WD radii and masses implies that the tidal strength and perihelion radius pairings in this work do not exactly match our previous models. Differences in the WD masses and equations of state will also affect the efficiency of nuclear reactions. We therefore do not expect to precisely duplicate our earlier results, but it is interesting and encouraging that they do not differ by much. For example, projecting our old results to the tidal strength standard $\beta \approx 4.5$, we find both of the non-rotating BH encounter scenarios considered in this work agree with the results from Paper 1 to roughly a factor of two in peak density, peak temperature, nuclear energy release, and element production.

The upgraded particle tracer capability introduced in this work allows us to evaluate the accuracy of the smaller 19-element inline nuclear reaction network by post-processing the traced thermodynamic state through a much larger 495-isotope network. The 19- and 495-isotope models agree extremely well: 20% on total energy release and calcium production, and better than a factor of two on iron production.

Black hole rotation has very little direct impact on nuclear activity at equivalent tidal strength parameterization, not more than 25% over the tidal strength range considered here, and very near the margin of numerical uncertainty. When orbital trajectories are adjusted for relativistic corrections by iterating on the perihelion radius until the WD mass centroids approach at comparable distances, there is little difference in the total energy release and in the final composition of burn products (iron and calcium group elements) even for near maximally rotating BHs with spin parameter $a = 0.9 M_{BH}$. This conclusion holds regardless of black hole mass or orientation of the spin axis relative to the orbital plane.

Prograde orbital motion has the potential to produce more unbound burn products compared to either non-rotating BHs or retrograde motion due to smaller ISCO and MBO radii that would allow closer encounters and thus more efficient nuclear burning and greater luminosity without material plunging immediately into the BH. As expected, we do find orders of magnitude greater iron production with close prograde encounters, culminating at about 50 (70)% mass conversion efficiency in total (unbound) mass elements. The mass ratio of unbound intermediate to iron group elements is also affected by prograde alignment, decreasing by orders of magnitude as increasingly more iron is produced from ever closer encounters made possible by decreasing marginally bound radii. The Ca/Fe mass ratio for example scales as $(\beta^*)^{-n}$ with $n \sim 4.3$ in both the near and far field debris over the range of relativistically corrected interaction strengths $5 \lesssim \beta^* \lesssim 9$. We additionally find unbound ^{56}Ni yields, and thus bolometric luminosities, scale roughly linearly with interaction strength over this same range. The events considered here give rise to lower peak luminosities (~ 0.74 - 4.7×10^{42} erg s^{-1}) than standard Ia events, aligning more closely with sub-luminous SN 1991bg and SNe Iax events.

Finally, tidal encounters between WD stars and intermediate black holes have been proposed as a potential source for observed calcium-rich gap transients (Holcomb et al. 2013; Sell et al. 2015). Recent observations of the gap transient system candidate SN-2016hnk (Sell et al. 2018), however, has raised doubts to this connection based on a lack of supporting X-ray emission expected from fall-back accretion immediately following the event. We nonetheless point out that our previous work did find a strong correlation between interaction strength and the ratio of intermediate

to iron group elements produced in a range of encounters. Calcium (iron)-rich debris was a natural outcome from relatively weak (strong) encounters, and the tidal strength proved to be an effective choking mechanism. Although we did not pursue a systematic study of this effect here, the strong dependency of burn product ratios on tidal strength is evident in these new models as well, particularly in the prograde series of calculations. One of the motivations for this work was to investigate whether BH spin or spin-orbit alignment might provide additional mechanisms for choking nuclear flows and producing incomplete burn environments. Our findings demonstrate this is not likely, at least for reasonable (less than maximal) rotation rates.

REFERENCES

Abbott, B. P., Abbott, R., Abbott, T. D., et al. 2016, Living Reviews in Relativity, 19, 1

Anninos, P., Fragile, P. C., Olivier, S. S., et al. 2018, ApJ, 865, 3

Anninos, P., Bryant, C., Fragile, P. C., et al. 2017, ApJS, 231, 17

Anninos, P., Fragile, P. C., & Salmonson, J. D. 2005, ApJ, 635, 723

Anninos, P., Fragile, P. C., Wilson, J., & Murray, S. D. 2012, ApJ, 759, 132

Arnett, W. D. 1979, ApJL, 230, L37

Brassart, M., & Luminet, J.-P. 2008, A&A, 481, 259

Camarda, K. D., Anninos, P., Fragile, P. C., & Font, J. A. 2009, ApJ, 707, 1610

Contardo, G., Leibundgut, B., & Vacca, W. D. 2000, A&A, 359, 876

Dado, S., & Dar, A. 2015, ApJ, 809, 32

Dong, X., Wang, T., Yuan, W., et al. 2007, ApJ, 657, 700

Evans, C., Laguna, P., & Eracleous, M. 2015, ApJ, 805, L19

Farr, W. M., Stevenson, S., Miller, M. C., Mandel, I., Farr, B. & Vecchio, A. 2017, Nature, 548, 426

Fragile, P. C., Gillespie, A., Monahan, T., Rodriguez, M., & Anninos, P. 2012, ApJS, 201, 9

Fragile, P. C., Olejar, A., & Anninos, P. 2014, ApJ, 796, 22

Fröhlich, C., Martínez-Pinedo, G., Liebendörfer, M., Thielemann, F.-K., Bravo, E., Hix, W. R., Langanke, K.-H., & Zinner, N. T. 2006, Phys. Rev. Lett. 96, 142502

Gafton, E. & Rosswog, S. 2019, ArXiv e-prints, arXiv:1903.09147

Gammie, C. F., Shapiro, S. L., & McKinney, J. C. 2004, ApJ, 602, 312

Gebhardt, K., Rich, R. M., & Ho, L. C. 2002, ApJL, 578, L41

—. 2005, ApJ, 634, 1093

Gerssen, J., van der Marel, R. P., Gebhardt, K., et al. 2002, AJ, 124, 3270

—. 2003, AJ, 125, 376

Haas, R., Shcherbakov, R. V., Bode, T., & Laguna, P. 2012, ApJ, 749, 117

Hartmann, D., Woosley, S. E., & El Eid, M. 1985, ApJ, 297, 837

Hoffman, R. D. & et al. 2010, ApJ, 715, 1383

Holcomb, C., Guillochon, J., De Colle, F., & Ramirez-Ruiz, E. 2013, ApJ, 771, 14

Kawana, K., Tanikawa, A., & Yoshida, N. 2017, MNRAS477, 3449

Lodders, K. 2003, ApJ, 591, 1220

Luminet, J.-P., & Carter, B. 1986, ApJS, 61, 219

Luminet, J.-P., & Pichon, B. 1989, A&A, 209, 103

MacLeod, M., Guillochon, J., Ramirez-Ruiz, E., Kasen, D., & Rosswog, S. 2016, ApJ, 819, 3

McClintock, J. E., Narayan, R., & Steiner, J. F. 2014, SSRv, 183, 295

Paxton, B., Bildsten, L., Dotter, A., et al. 2011, ApJS, 192, 3

Pruet, J. & et al. 2006, ApJ, 644, 1028

Rauscher, T. & Thielemann, F. 2001, At. Data Nucl. Data Tables, 75, 1

Rees, M. J. 1988, Nature, 333, 523

Reynolds, C.-S. 2014, SSRv, 183, 277

Rosswog, S., Ramirez-Ruiz, E., & Hix, W. R. 2009, ApJ, 695, 404

Seitenzahl, I. R., Meakin, C. A., Townsley, D. M., Lamb, D. Q., & Truran, J. W. 2009, ApJ, 696, 515

Sell, P. H., Maccarone, T. J., Kotak, R., Knigge, C., & Sand, D. J. 2015, MNRAS, 450, 4198

Sell, P. H., Arur, K., Maccarone, T. J., Kotak, R., Knigge, C., Sand, D. J., & Valenti, S. 2018, MNRAS, 475, L111

Stone, N., Sari, R., & Loeb, A. 2013, MNRAS, 435, 1809

Suntzeff, N. B. 2002, in From Twilight to Highlight, The Physics of Supernovae, ed. W. Hillebrandt, B. Leibundgut, 183

Tanikawa, A., Sato, Y., Nomoto, K., et al. 2017, ApJ, 839, 81

Thorne, K.-S. 1974, ApJ, 191, 507

Timmes, F. X., Woosley, S. E., Hartmann, D. H., & Hoffman, R. D. 1996, ApJ, 464, 332

Timmes, F. X. 1999, ApJS, 124, 241

Timmes, F. X., & Swesty, F. D. 2000, ApJS, 126, 501

Timmes, F. X., Hoffman, R. D., & Woosley, S. E. 2000, ApJS, 129, 377

Weaver, T. A., Zimmerman, G. B., & Woosley, S. E. 1978, ApJ, 225, 1021

Woosley, S. E. 1986, in Nucleosynthesis and Chemical Evolution, ed. B. Hauck, A. Maeder, G. Meynet, 74